

● *Original Contribution***BONE SURFACE LOCALIZATION IN ULTRASOUND USING IMAGE  
PHASE-BASED FEATURES**ILKER HACIHALILOGLU,\* RAFAEF ABUGHARBIEH,\* ANTONY J. HODGSON,<sup>†</sup> and ROBERT N. ROHLING\*<sup>†</sup>

\*Department of Electrical and Computer Engineering, University of British Columbia, Vancouver, BC, Canada; and

<sup>†</sup>Department of Mechanical Engineering, University of British Columbia, Vancouver, BC, Canada

(Received 31 March 2008, revised 1 April 2009, in final form 18 April 2009)

**Abstract**—Current practice in orthopedic surgery relies on intraoperative fluoroscopy as the main imaging modality for localization and visualization of bone tissue, fractures, implants and surgical tool positions. Ultrasound (US) has recently emerged as a potential nonionizing imaging alternative that promises safer operation while remaining relatively cheap and widely available. US images, however, often depict bone structures poorly, making automatic, accurate and robust localization of bone surfaces quite challenging. In this paper, we present a novel technique for automatic bone surface localization in US that uses local phase image information to derive symmetry-based features corresponding to tissue/bone interfaces through the use of 2-D Log-Gabor filters. We validate the performance of the proposed approach quantitatively using realistic phantom and *in vitro* experiments as well as qualitatively on *in vivo* data. Results demonstrate that the proposed technique detects bone surfaces with a localization mean error below 0.40 mm. Furthermore, small gaps between bone fragments can be detected with fracture displacement mean error below 0.33 mm for vertical misalignments, and 0.47 mm for horizontal misalignments. (E-mail: [rafeef@ece.ubc.ca](mailto:rafeef@ece.ubc.ca)) © 2009 World Federation for Ultrasound in Medicine & Biology.

**Key Words:** Local phase features, Phase symmetry, Log-Gabor filters, Ultrasound imaging, Bone segmentation, Fracture detection, Orthopaedic surgery.

**INTRODUCTION**

Two-dimensional fluoroscopic imaging has long been used as the primary intraoperative modality in orthopedic surgery because of its relatively clear depiction of bone surfaces, fractures, implants and surgical tools. However, with such projection imaging, surgeons typically face considerable difficulties in accurately localizing bone fragments in 3-D space and assessing the adequacy and accuracy of reduced fractures. Surgical procedures are thus highly dependent on the experience of the surgeon and prone to trial and error. Furthermore, fluoroscopy involves significant radiation exposure potentially harmful to both patients and surgical teams, with the latter enduring repeated exposure on a regular basis. Researchers have recently started to investigate possible alternative imaging modalities for such surgical tasks, with US imaging emerging as a primary candidate (Amin et al. 2003; Barratt et al. 2006; Beek et al. 2007;

Kryvanos 2002; Penney et al. 2006; Tonetti et al. 2001). US image data, however, is typically characterized by high levels of speckle noise, reverberation, anisotropy and signal dropout, which introduce significant difficulties in interpretation of captured data, automatic detection of image features and accurate localization of imaged bone surfaces (Brendel et al. 2002; Jain and Taylor 2004). In particular, the appearance of bone surfaces in US remains strongly influenced by beam direction and regions corresponding to bone boundaries appear blurry (Fig. 1).

US imaging has the potential of providing a powerful new tool for practical and real-time guidance during orthopaedic surgery as long as anatomical structures of interest can be visualized and localized with sufficient accuracy and efficiency. Our particular clinical research interest is mainly in orthopedic fracture surgeries, with our main focus being on bone fractures of the distal radius, which are responsible for about one sixth of all fractures seen in emergency departments in the United States (Hanel et al. 2002; McMurtry et al. 1997), and fractures of the pelvis (Coppola and Coppola 2000). Adequate accuracy in reduction is critically needed in such applications to avoid malunions that can lead to radiocarpal and

Address correspondence to: Dr. Rafeef Abugharbieh, Dept. of Electrical and Computer Engineering, 2332 Main Mall, UBC, Vancouver, BC, V6T 1Z4, Canada. E-mail: [rafeef@ece.ubc.ca](mailto:rafeef@ece.ubc.ca)

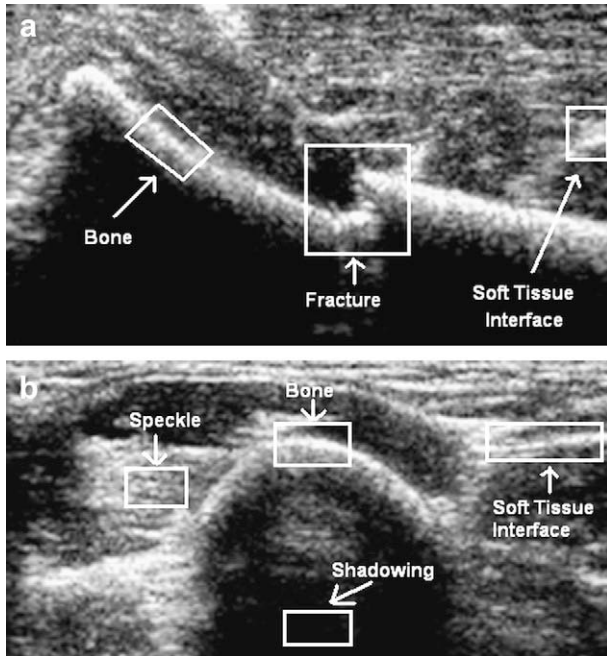


Fig. 1. Examples of 2-D US images acquired. (a) Phantom Sawbone with bovine soft tissue overlaid on top. (b) *In vivo* distal radius. Regions within white rectangles highlight typical bone responses and common artefacts in bone US. Note the highly realistic nature of our phantom data in (a) and its close likeness to real *in vivo* data in (b).

radioulnar pain and diminished range of motion for distal radius fractures, or pain syndromes and leg-length discrepancies for pelvic fractures.

Employing US imaging in orthopaedic surgery has been reported in the past (Tonetti et al. 2001; Barratt et al. 2006; Beek et al. 2007), though analysis remained mainly manual, which is prohibitively time consuming, tedious and prone to significant inter- and intrauser variability. Several attempts to automate US image segmentation in various applications have nonetheless been proposed. Traditional methods based on image intensity and local gradient information are common (Daanen et al. 2004; Kowal et al. 2007; Kryvanos 2002), but results remain unpredictable and highly sensitive to parameter setting. To increase robustness, some researchers proposed incorporating *a priori* bone appearance information into the segmentation framework, e.g., (Daanen et al. 2004; Jain and Taylor 2004) and (Alfiansyah et al 2006; He and Zheng 2001); they used active shape models, hence combining shape models with intensity and gradient information. However, fractured bone surfaces often significantly violate prior assumptions, making such an approach not feasible.

Image phase information has been previously used for processing US images of soft tissue. Examples include magnetic resonance to US data registration (Mellor and Brady 2005), ultrasound compounding for echocardiography

image enhancement (Grau and Noble 2005), endocardial border detection and image enhancement in 3-D echocardiography (Boukerroui et al. 2001; Mulet-Parada and Noble 2000; Sanchez-Ortiz et al. 2000; Ye and Noble 2002) and liver characterization (Cao et al. 2006). However, to the best of our knowledge, phase-based image features have never before been applied to bone US nor were directed at assessing bone fractures. In a recent preliminary work (Haciha-liloglu et al. 2006) we investigated the potential of using local phase-based image features for bone localization in US data. In this study we propose and evaluate the novel use of phase symmetry features derived from US images using 2-D Log-Gabor filters for automatic segmentation of bone surfaces and fracture detection. We also present extensive validation studies using carefully designed phantom, *in-vitro* and *in vivo* experiments, and demonstrate the accuracy and robustness of our proposed approach.

## METHODS AND MATERIALS

Image phase information is a key component in the interpretation of a scene that has long been known to contribute more to the visual appearance of an image than magnitude information (Oppenheim and Lim 1981). In a seminal paper, Morone and Owens (1987) proposed the use of a local energy model for phase-based feature detection, where they argued that features are perceived at points in the signal where the Fourier components are maximally in phase, *i.e.*, where phase congruency (PC) is maximal. Since then, phase information has been widely investigated as a basis for feature extraction in various image data (Grau and Noble 2005; Kovesi 1996, 1997; Mulet-Parada and Noble 2000; Sanchez-Ortiz et al. 2000). In this work, we propose using local phase information as a powerful, yet simple, novel approach for accurate and robust feature detection in US images of bony structures.

### Local phase-based image features

Quadrature filters can be used to capture local signal properties through the calculation of signal amplitude and phase at a particular scale (frequency) at a given spatial location. A popular choice of quadrature filters is the Log-Gabor filter (Field 1987; Kovesi 1996), which is defined in the frequency domain as in eqn (1) (note that equations for a 1-D signal are shown for simplicity):

$$G(\omega) = \exp\left(-\frac{(\log(\omega/\omega_0))^2}{2(\log(\kappa/\omega_0))^2}\right) \quad (1)$$

where  $\kappa$  is a scaling factor and  $\omega_0$  is the center frequency of the filter. The ratio of these two variables is related to the filter's bandwidth ( $\beta$ ) (Boukerroui et al. 2004) as in eqn (2):

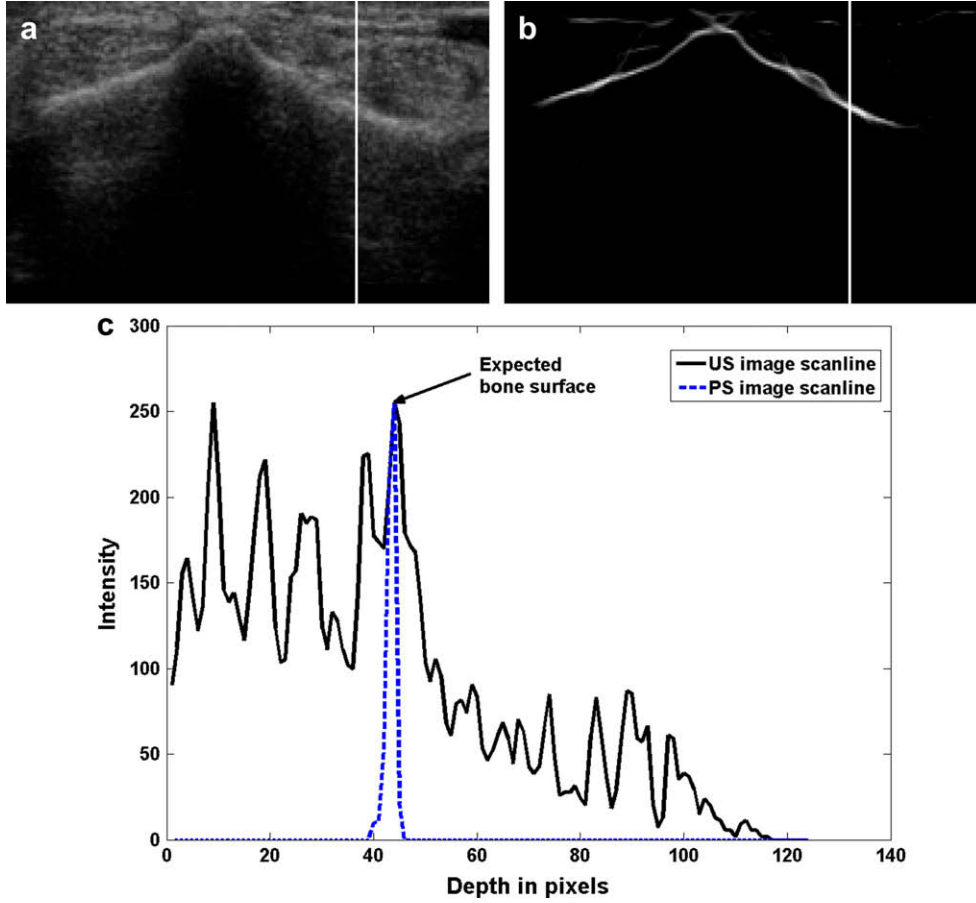


Fig. 2. Illustration of the bone response in original and processed US images with an example (vertical) line profile shown. (a) Original 2-D *in vivo* image of a human distal radius (US probe is pointing top to bottom in the image). (b) Corresponding phase symmetry *PS* image obtained using our proposed phase based feature. (c) Example line profile across the bone surface in (a) shown in solid black, and across that in (b) shown in dashed blue. Note how the *PS* profile shows a high peak at the expected bone surface location (indicated by the arrow on the ridgelike bone profile in US). Note how *PS* facilitates robust detection of the bone edge, even in the presence of many different edge responses that are a result of the soft tissue interface and associated US artefacts.

$$\beta = -\frac{2\sqrt{2}}{\sqrt{\ln 2}} \ln(\kappa/\omega_0). \quad (2)$$

Simultaneous localization of spatial and frequency signal information can therefore be obtained by constructing a filter bank using a set of quadrature filters created from rescalings of the reference Log-Gabor filter. The filter bank is constructed at different scales that are multiples of a minimum user-defined wavelength,  $\lambda_{\min}$ . Let the signal to be analyzed be  $I(x)$ , and let  $M_m^e(x) = \text{real}(F^{-1}(G(\omega)))$  and  $M_m^o(x) = \text{imag}(F^{-1}(G(\omega)))$  denote the even and odd Log-Gabor filters at a scale  $m$ , where  $F^{-1}$  denotes the inverse Fourier transform operation. The amplitude  $A_m(x)$ , local phase  $\phi_m(x)$  and the local energy function  $E(x)$  at a given filter scale ( $m$ ) can then be calculated as in eqn (3):

$$\begin{aligned} A_m(x) &= \sqrt{e_m(x)^2 + o_m(x)^2}; \phi_m(x) = \tan^{-1}(o_m(x), e_m(x)); \\ E(x) &= \sqrt{\left(\sum_m e_m(x)\right)^2 + \left(\sum_m o_m(x)\right)^2}, \end{aligned} \quad (3)$$

where  $e_m(x) = I(x) * M_m^e(x)$ ,  $o_m(x) = I(x) * M_m^o(x)$ . Accordingly, at each point  $x$  in the signal  $I(x)$ , different responses for each scale of the Log-Gabor filter can be obtained. These responses form the basis of a localized representation of the signal as we describe next.

#### Proposed US image features for bone localization

In US images, bone surfaces typically appear blurred, with nonuniform intensity and substantial shadowing beneath the surface. A line profile across the bone surface in fact reveals that the US response depicts

a ridgelike rather than a step or ramplike edge at the bone boundaries (Fig. 2). We therefore propose the use of a ridge detector as a sensitive feature for bone surface localization in US. The purpose of ridge detection is to capture the major axis of symmetry. Signals that have even symmetry about the origin will have real (and even) Fourier transforms, whereas signals that have odd symmetry will have imaginary (and odd) Fourier transforms. Signals that are neither perfectly odd nor perfectly even will have complex Fourier transforms, with the corresponding phase values reflecting their degree of symmetry. Using local phase information, as calculated in eqn (3), a point of symmetry will thus result in the response of the even filter ( $e_m(x)$ ) dominating the response of the odd filter ( $o_m(x)$ ) (Kovesi 1997). By taking the difference of these responses over a number of scales, a measure of phase symmetry ( $PS$ ) can then be defined as in eqn (4) (Kovesi 1997):

$$PS(x) = \frac{\sum_m [|e_m(x)| - |o_m(x)|] - T}{\sum_m \sqrt{e_m(x)^2 + o_m(x)^2} + \epsilon}, \quad (4)$$

where  $[A] = \max(A, 0)$ ,  $\epsilon$  is a small number included to avoid division by zero and  $T$  is a noise threshold calculated as a specified number ( $k$ ) of standard deviations ( $\sigma$ ) above the mean ( $\mu$ ) of the local energy distribution because of noise (Kovesi 1999).  $T$  is defined as:  $T = \mu + k \sigma$  (Kovesi 1999). The response of the smallest scale filter is used to estimate  $\mu$  and  $\sigma$  because it has the largest bandwidth and will give the strongest noise response. For different US machine settings and for different sequences,  $k$  can be tuned to provide a balance between the detected bone surface and speckle scale. At the tissue/bone interface, the  $PS$  value will be shown

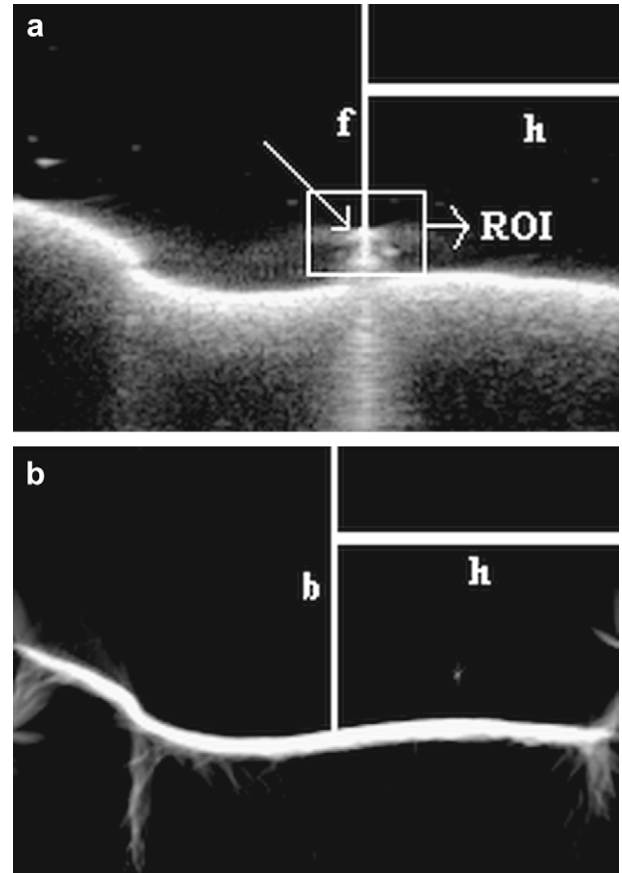


Fig. 3. Experiment 1: Bone surface localization measurements using a 3-mm bead. (a) Original US image. (b) Corresponding  $PS$  feature image. For each vertical profile (at position  $h$ ), the measurements  $f$  and  $b$  are made from US and  $PS$  images.  $PS$  measurements are considered accurate when  $b$  approaches  $f+3\text{mm}$ .

later in the paper to be much higher compared with the  $PS$  values obtained from soft tissue interfaces and US artifacts.

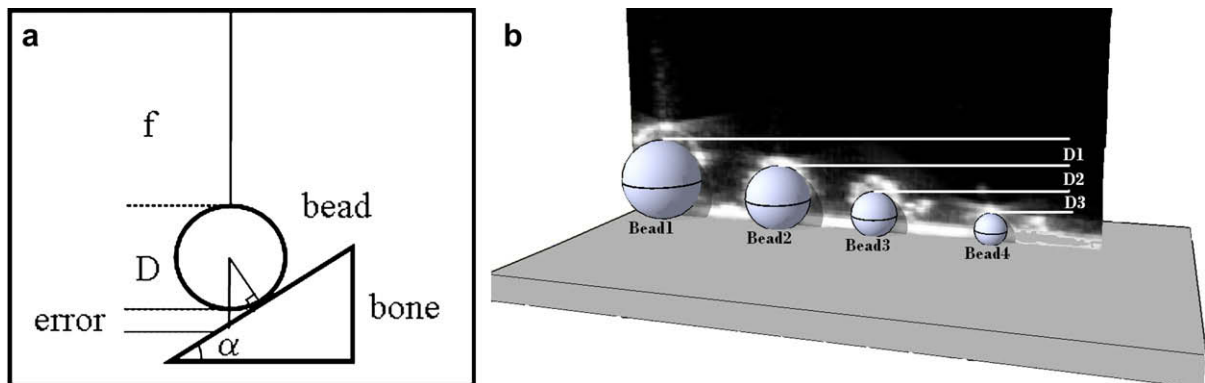


Fig. 4. Testing different bead radii in experiment 1. (a) For cases where the bone surface is angled by  $\alpha=20^\circ$ , a geometric error is induced in the estimation of the bone surface because the bead does not touch the surface along the vertical measurement direction. This error is calculated and added to the measurements. (b) A series of US images were acquired with four beads of decreasing diameter.  $D1$  is the difference in diameter between beads 1 and 2,  $D2$  is the difference between beads 2 and 3 and  $D3$  is the difference between beads 3 and 4. The appearance of the echo from the top surface of each bead should decrease by the difference in diameters to the next smaller bead.



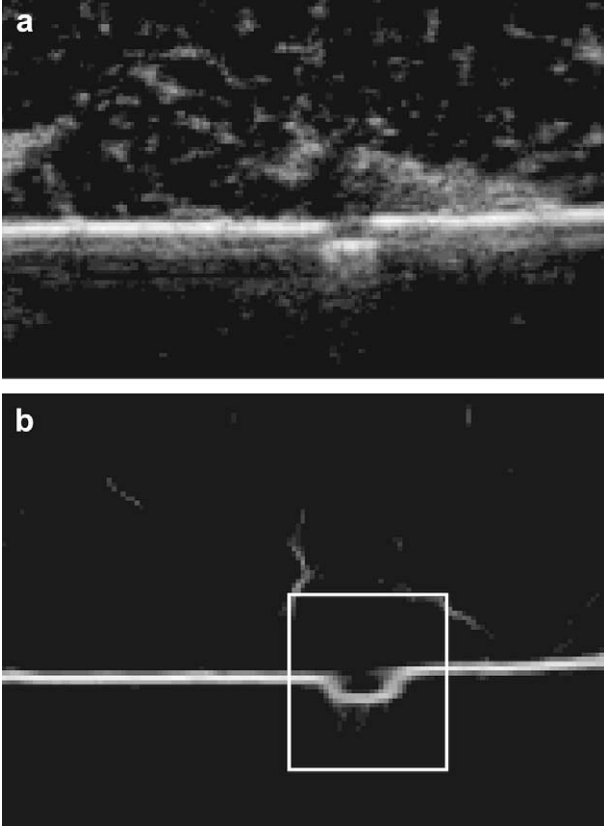


Fig. 5. Measurement of horizontal displacement of bone fragments in experiment 2. (a) US image with soft tissue overlaid on the Sawbone. (b) Corresponding *PS* image showing the ROI selected for the subpixel edge detection.

To extend the analysis into 2-D for our US images, our feature detection is performed at a number of separate orientations ( $r$ ), with the results subsequently combined. Accordingly, orientable 2-D filters are defined by spreading a Log-Gabor function into two dimensions, where a filter tuned to a particular orientation  $\phi_0$  is constructed by masking a radial Log-Gabor function with an angular Gaussian tuned to  $\phi_0$ . The radial component controls the frequency band to which the filter responds, and the angular component controls the orientation to which the filter responds. The resulting two components are then combined into a 2-D Log-Gabor function as in eqn (5):

$$G(\omega, \phi) = \exp \left[ - \left( \frac{(\log(\omega/\omega_0))^2}{2(\log(\kappa/\omega_0))^2} + \frac{(\phi - \phi_0)^2}{2\sigma_\phi} \right) \right]. \quad (5)$$

Here  $\sigma_\phi = \Delta\phi/s$  defines the angular bandwidth  $\Delta\Omega$  given as:

$$\Delta\Omega = 2 \times \sigma_\phi \sqrt{2 \times \log 2}, \quad (6)$$

where  $\Delta\phi$  is the angular separation between neighboring orientations and is defined as  $\Delta\phi = 180^\circ/N_r$ , where  $N_r$

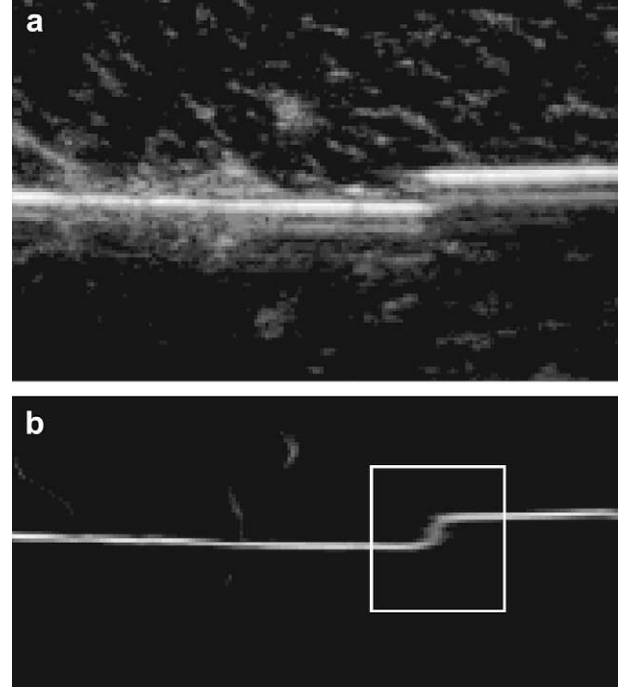


Fig. 6. Measurement of vertical displacement of bone fragments in experiment 2. (a) US image with soft tissue overlaid on the Sawbone. (b) Corresponding *PS* image showing the region of interest ROI selected for the subpixel edge detection.

denotes the total number of orientations used. The parameter  $s$  controls the angular overlap of the filter's transfer function. We empirically found that setting  $N_r = 6$  ensured even spectral coverage of the spectrum with a sufficient number of bone surface response directions tested. Increasing the number of orientations, in our experience, had little effect on the quality of the outcome but increased the computational complexity of the algorithm. Our angular bandwidth was set to  $25^\circ$ , which corresponds to  $s = 1.2$ . During the construction of the angular component of the filter,  $\sigma_\phi$  should be kept small to ensure good orientation resolution. On the other hand, the angular component should contain an adequate range of frequencies to ensure its robustness to noise (setting  $s = 1.2$  ensured that this compromise was met). By using the above 2-D filter over a number of scales ( $m$ ) and at different orientations ( $r$ ), a 2-D *PS* measure can then be defined as in eqn (7):

$$PS(x, y) = \frac{\sum_r \sum_m [|e_{rm}(x, y)| - |o_{rm}(x, y)|] - T_r}{\sum_r \sum_m \sqrt{e_{rm}^2(x, y) + o_{rm}^2(x, y)} + \varepsilon}. \quad (7)$$

The orientation-dependent noise threshold  $T_r$  is calculated as previously explained (for the 1-D case), however, with the response of the smallest scale filter belonging to a specific orientation being used which allows for the calculation of an independent noise compensation

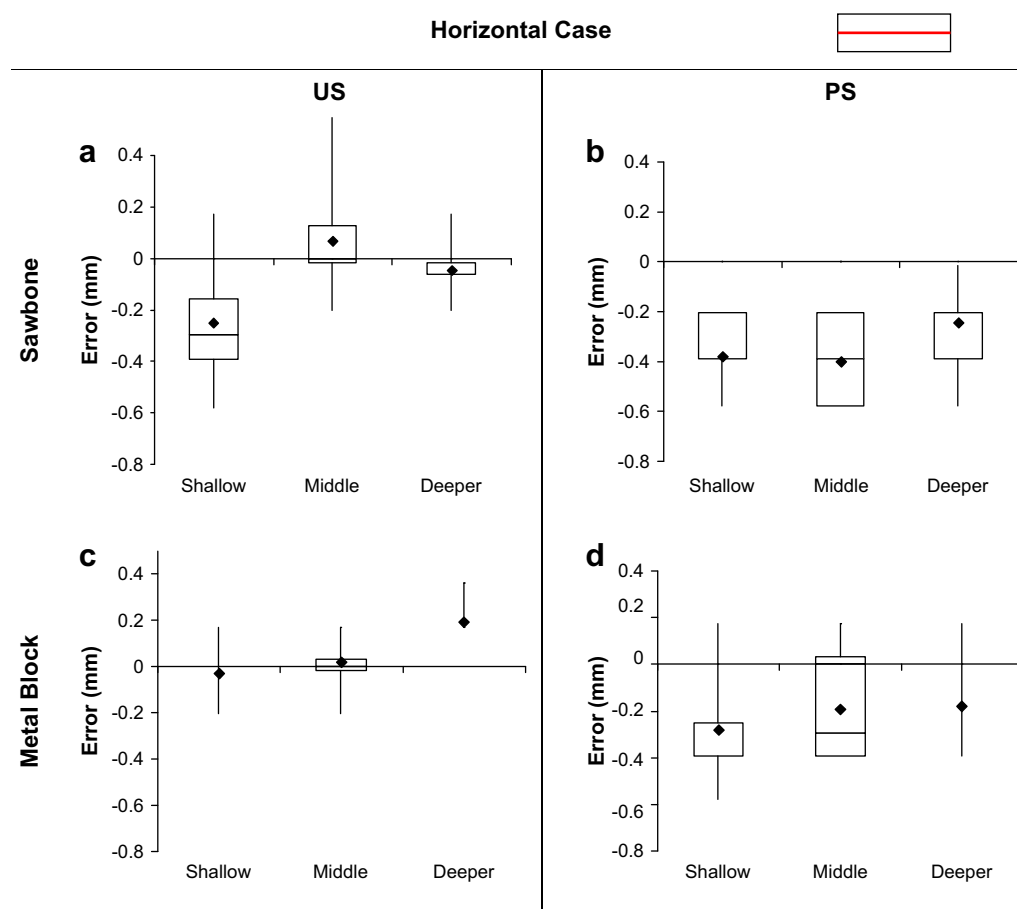


Fig. 7. Bone surface localization errors for a horizontal surface in a water bath in experiment 1. Errors are calculated as the difference between the edge-detector results and the results from the bead location. Tests were repeated for the phantom near the top, middle and bottom of the US image. (a) US image used in edge-detection on a Sawbone. (b) PS image used in edge-detection on a Sawbone. (c) US image used in edge-detection on a flat metal block. (d) PS image used in edge-detection on a flat metal block. The black point represents the mean, and the box and whiskers represent the standard deviation and range of the data.

term for each orientation. Figure 2 demonstrates our proposed processing approach and shows an example line profile across the bone surface obtained from the extracted PS image overlaid on top of the corresponding profile in the original US image. It can be clearly seen that the PS image has a maximum at the bone boundary.

#### Data acquisition and experimental setup

A number of carefully designed experiments were used to evaluate the performance of our proposed phase-based US data processing method; the first experiment quantitatively tested the accuracy of bone surface localization, the second quantitatively assessed accuracy of measuring gaps between bone fragments and the third investigated qualitative results. The acquisition system consisted of an US scanner (Voluson 730, GE Healthcare, Waukesha, WI) with a 3D RSP5-12 probe. A tracking system (OPTOTRAK 3020, Northern Digital Inc., Waterloo, ON, Canada) was used to generate the gold

standard measurement of relative bone fragment displacements. The acquired US volumes (each comprising cubic voxels of 0.19mm) were transferred from the US machine to a computational workstation using 3DView2000, a propriety software package from GE Medical Systems.

#### Experiment 1—Accuracy assessment of bone surface localization

In this experiment, we compared the surface localization accuracy obtained from both the original B-mode US image and the proposed PS feature image to the “gold standard” measurement of the surface made with a stylus whose 3-mm diameter spherical tip was visible in the US image. The echo from this tip was determined to be accurate down to a subpixel resolution, as will be shown later, so the bone can be considered to lie 3 mm distal to the near side of the spherical tip.

Two surface models were used: a flat metal block and a Sawbone model (#1018-3, Sawbones Inc., Vashon

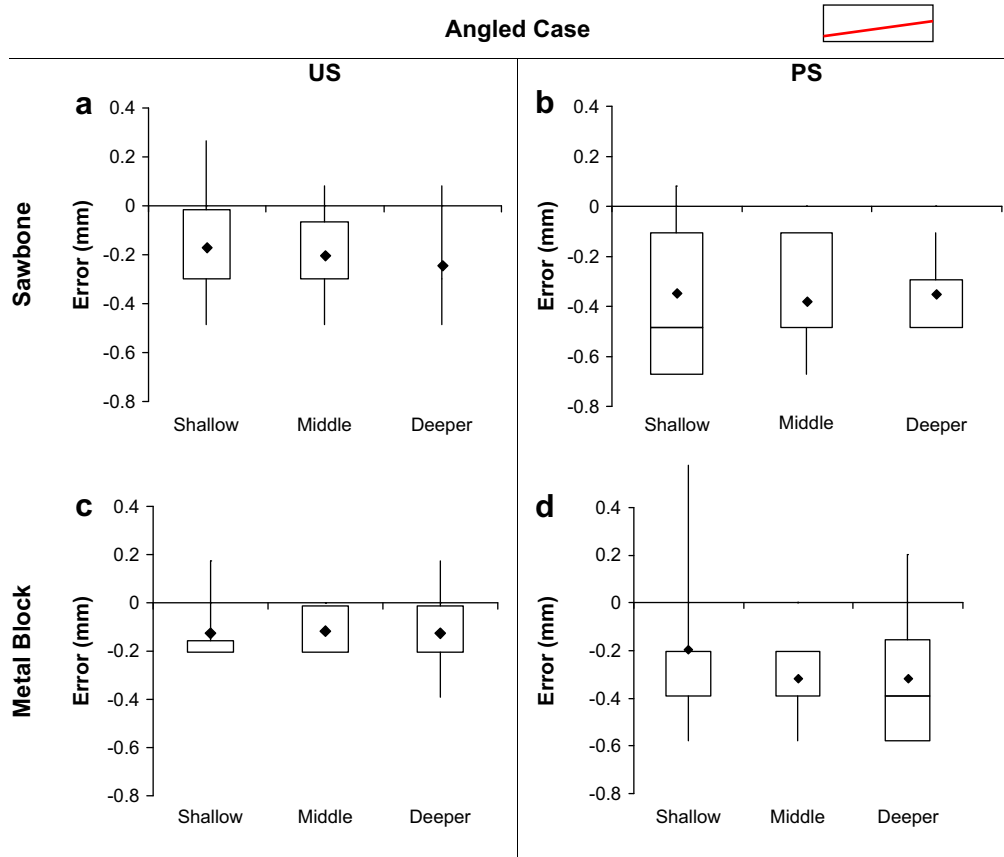


Fig. 8. Bone surface localization errors for a surface angled  $\alpha = 20^\circ$  in a water bath in experiment 1. Errors were calculated as the difference between the edge-detector results and the results from the bead location. Tests were repeated for the phantom near the top, middle and bottom of the US image. (a) US image used in edge-detection on a Sawbone. (b) PS image used in edge-detection on a Sawbone. (c) US image used in edge-detection on a flat metal block. (d) PS image used in edge-detection on a flat metal block. The black point represents the mean, and the box and whiskers represent the standard deviation and range of the data.

WA, USA). Each model was immersed inside a water-filled tank, with the long axis of the model aligned with the scan plane to the best of the operator's ability. Images were obtained at three different depths by raising or lowering the probe position inside the water tank and realigning the model at each depth to ensure it was centered in the elevation direction. Two orientations of the model were also tested; horizontal and inclined at  $20^\circ$ , which we consider to be an upper limit for longitudinal angulation in the clinical situations for which we intend to use this imaging technique. At each orientation and depth, the bead was scanned at 15 different locations along the model surface. To ensure that the bead was centered in the beam direction, the position of the stylus was adjusted until the clearest possible surface reflection was obtained.

The location of the bright intensity response from the top of the bead tip,  $f$ , in the US image, and the location of the intensity response of the model surface obtained from the PS image,  $b$ , were then extracted, as shown in Fig. 3, using an automated algorithm to reduce operator-related

variability. First, a region-of-interest (ROI) was selected by the user around the bead top surface. A subpixel edge detection algorithm then automatically detected the top surface of the bead within the ROI by locating the position with the maximum vertical gradient. The same edge detection algorithm was also used to detect edges of the model surface in the PS image. The model surface localization error (in mm) was therefore defined as:  $error = D - (b - f) * \text{pixel length}$ , where  $D$  is the bead diameter. In the inclined orientation case, we corrected for the geometric error resulting from the bead not touching the surface along the vertical measurement direction (Fig. 4) as in eqn (8):

$$\cos\alpha = \frac{D/2}{D/2 + error_\alpha} \Rightarrow error_\alpha = \frac{D/2}{\cos\alpha} - D/2. \quad (8)$$

A  $20^\circ$  angle produced an error of 0.096 mm, which was added to  $f$ . Some error may also arise from the squint angle of the transducer, but this error is assumed

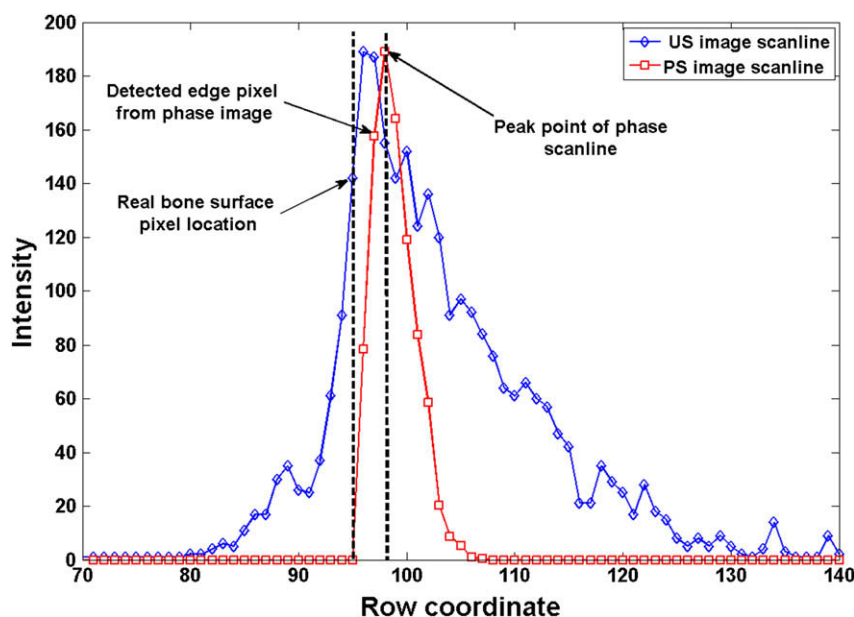


Fig. 9. Sample scanline profile through the bone surface in the original US image (*blue*) and proposed *PS* (*red*) images. The two vertical dotted lines correspond to the pixel preceding the first positive intensity (line to the left) and the maximum intensity (line to the right) value of the line profiles. The real bone location lies close to the dotted line on the left, suggesting that the location where the gradient of *PS* is maximal corresponds to the true bone surfaces.

to be negligible for the range of bead diameters used in the tests. This error is less than 0.01 mm for a squint angle of  $2^\circ$  and less than 0.1 mm for a squint angle of  $10^\circ$ ; the actual squint angle is assumed to be much less than  $10^\circ$ .

Our accuracy tests assume that the sphere surface detected in the B-mode US image is in fact located at the top of the sphere (or at least at a small fixed offset) rather than at some interior or exterior point that depends on the radius of the sphere. To confirm the validity of our assumption, a separate validation step was conducted in which US images were acquired with a selection of *differently-sized beads* (with 1.5 mm, 3.2 mm, 4.3 mm and 6.3 mm radius, respectively) glued against a metal block (Fig. 4) and immersed in water. B-mode US scans were obtained at three different depths (10 repetitions at each depth), with the same previously described edge detection algorithm used to locate the top of each bead. The differences in depth measurements between the surfaces of all possible pairs of beads were compared against the actual known differences in bead diameter.

#### Experiment 2—Accuracy assessment of bone fracture measurement

An important capability in an orthopaedic surgery system for fracture assessment is the ability to easily identify bone fragments and accurately assess their reduction. Our second experiment was thus designed to evaluate the accuracy of using the proposed *PS* features in measuring gaps between bone fragments.

The Sawbone model was cut into two parts, with each part glued to the top surface of a metal block. Infrared emitting diodes were glued to the surface of one of the metal blocks to allow tracking of the displacements by an OPTOTRAK system. One block remained fixed and the other block was moved and clamped at different displacements and both vertical and horizontal displacements were measured. The OPTOTRAK, which was used to provide the gold standard displacement measurements, has a reported RMS accuracy of 0.1 mm in the *x* and *y* (lateral) directions, and 0.15 mm in the *z* (depth) direction at a distance of 2.5 m (Rohling et al. 1995). The range of displacements tested varied between  $\approx 0.6$ –2.2 mm. Continuous OPTOTRAK measurements verified that the displaced fractures remained stationary during US imaging. Tests were conducted first with standard coupling gel and then repeated with a 2-cm-thick slice of bovine muscle tissue overlaid on top of the fracture to simulate more realistic specimen conditions. The bovine tissue was obtained through a certified butcher following guidelines and notification of the UBC Animal Care and Biosafety Committee. A total of 10 scans were obtained for each displacement and the resulting measurements of the displacement from the *PS* image were compared with those measured by the OPTOTRAK system. The measurements in the image space were done by first applying the previously described subpixel edge detection (experiment 1) on a selected ROI around the fracture in the *PS* image and then measuring the distance between the detected edges on each side of the



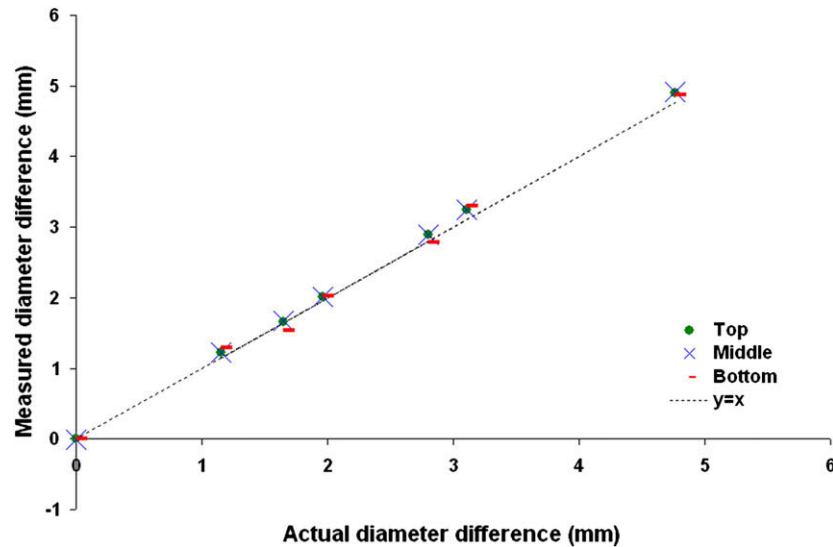


Fig. 10. Validation of bead measurements in experiment 1. If the edge measurements from the US images correspond to the top of the bead, then the difference in measurements from one bead to a smaller bead should be equal to the difference in the bead diameters. The measured differences between bead diameters is thus plotted against the actual differences in diameters. Tests were repeated for the bead near the top, middle and bottom of the image. The plot shows that data closely follows the  $y = x$  line, indicating good agreement.

fragment. For horizontal displacements, this was performed by measuring the horizontal distance between the two closest edge pixels that lie along the gap (Fig. 5). The same method was used for measuring vertical displacements (Fig. 6). Measurement error was defined as the displacement measured from the *PS* image subtracted from the displacement obtained from the OPTOTRAK.

#### Experiment 3—Qualitative evaluation using *in vivo* specimens

For qualitative evaluation of the proposed bone localization method, tests were performed *in vivo* on the distal radius and ulna of a normal volunteer, as well as on the Sawbone model overlaid with  $\sim 2.5$  cm of bovine tissue. Because most previous work on bone localization in US used gradient or edge-based segmentation methods, we also applied gradient calculations and Canny edge detection to compare with the *PS* image results. The parameters of the gradient and Canny calculations were adjusted empirically for each image to give the best appearance.

## RESULTS AND DISCUSSION

For each experiment, the phase images were calculated as in eqn (7) using empirically determined filter parameters. A set of scales ( $m = 2$ ) and orientations ( $N_r = 6$ ), with  $\kappa/\omega_0 = 0.25$  and a filter wavelength of  $\lambda_{\min} = 25$  pixels, were used, which offered good spectral coverage and orientation resolution and produced good bone surface localization in the presence of speckle. The

noise threshold parameter  $k$  was set to 8. Throughout the experiments, these values were *not* changed.

#### Experiment 1—Bone surface localization

The processing time for the *PS* calculation for each 2-D US image was approximately 0.5 s on an Intel Pentium 4 PC (3.64 GHz, 2 GB of RAM). Box and whisker plots of the localization errors from both US and *PS* images are shown in Fig. 7 for horizontal Sawbones and metal blocks. Figure 8 shows box and whisker plots for the angled case. The simpler surface geometry of the metal block produced smaller errors than the Sawbone for both cases.

The model surface estimated using the *PS* image tended to lie slightly interior to the bone on both models (metal block: mean =  $-0.28$  mm with std = 0.27; Sawbone model: mean =  $-0.34$  mm with std = 0.16 relative to the gold standard estimate of 3 mm distal to the edge of the sphere detected in the B-mode US image). The point of maximum gradient on the proximal edge was also a closer match to the gold standard estimate (Fig. 9). The surface detected directly from the B-mode image had no significant bias (mean =  $-0.11$  mm with std = 0.2).

In both horizontal and inclined measurements, whether obtained from US or from *PS* images, the mean error was calculated based on measurements taken at 15 different bead locations for each depth setting. Hereafter, we will report the highest mean error results of these three different depth settings as “maximum mean error.” For the Sawbone model, the maximum mean error from US was 0.25 mm inside the Sawbone surface when the surface

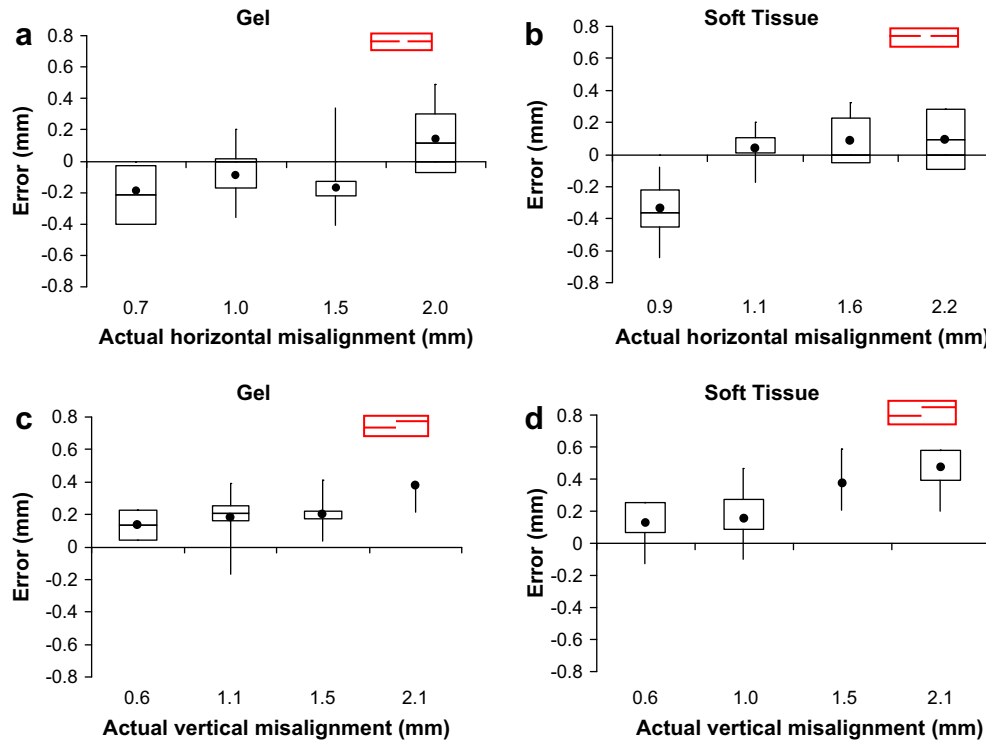


Fig. 11. Horizontal and vertical displacement measurement errors from a fractured Sawbone in experiment 2. “Gel” indicates that the US transmission medium was coupling gel, and “Soft Tissue” indicates that a layer of bovine muscle tissue was used. The error was defined as the difference between the measurements from *PS* and the OPTOTRAK. (a) Horizontal displacement with coupling gel. (b) Horizontal displacement with soft tissue. (c) Vertical displacement with coupling gel. (d) Vertical displacement with soft tissue.

was horizontal and 0.26 mm when angled. The maximum mean error from *PS* was 0.40 mm inside the bone surface when horizontal and 0.38 mm when angled. These tests were performed in a water bath, so both US and *PS* show a high level of accuracy that is independent of the angle of the surface in this range and independent of the depth. It should be noted that the ability to detect the bone surface directly from US is relatively easy in a water bath, but images of real tissue will contain significant artefacts. Edge detection in US is also more sensitive to parameter adjustment; the values used here to achieve the highest accuracy later proved unsuitable for *in vivo* tests and had to be readjusted empirically. The *PS* results are less sensitive to parameter setting, where the same parameter values were found suitable both for water tank and *in vivo* tests.

Figure 10 confirms that the top surface of the bead response does indeed drop by the difference in bead diameters for different beads. This suggests that the edge detector is identifying the top of the bead, with at most a constant bias that is independent of bead diameter. No statistically significant difference was found between the actual differences of bead diameter and measured diameter for all locations in the image (paired student *t*-test,  $p = 0.90$ ).

#### Experiment 2—Bone fracture displacement

Box and whisker plots of the errors from horizontal and vertical displacements are shown in Fig. 11 for both gel and soft tissue mediums. The errors in estimating displacements were consistently small, with maximum mean errors under 0.5 mm for all tests (here again “maximum mean error” indicates the mean error result that had the highest error among the introduced displacements). These results are especially encouraging for the potential use of *PS* in fracture assessment because the accuracy required in surgical navigation systems is typically in the range of 2–4 mm (Phillips 2007).

#### Experiment 3—Qualitative results

Figure 12 shows qualitative bone localization results on *in vivo* scans of the human radius and ulna obtained using *PS* and compared with results of standard Canny and gradient images. For the gradient calculations, a 2-D Gaussian with a standard deviation of two pixels for both directions was used for all scans. For the Canny edge detector, a threshold value of 90% and standard deviation of 2 pixels was used. These parameters were changed to 80% threshold value and a standard deviation of three pixels for the *in vivo* scans to obtain good results with minimal artifacts.

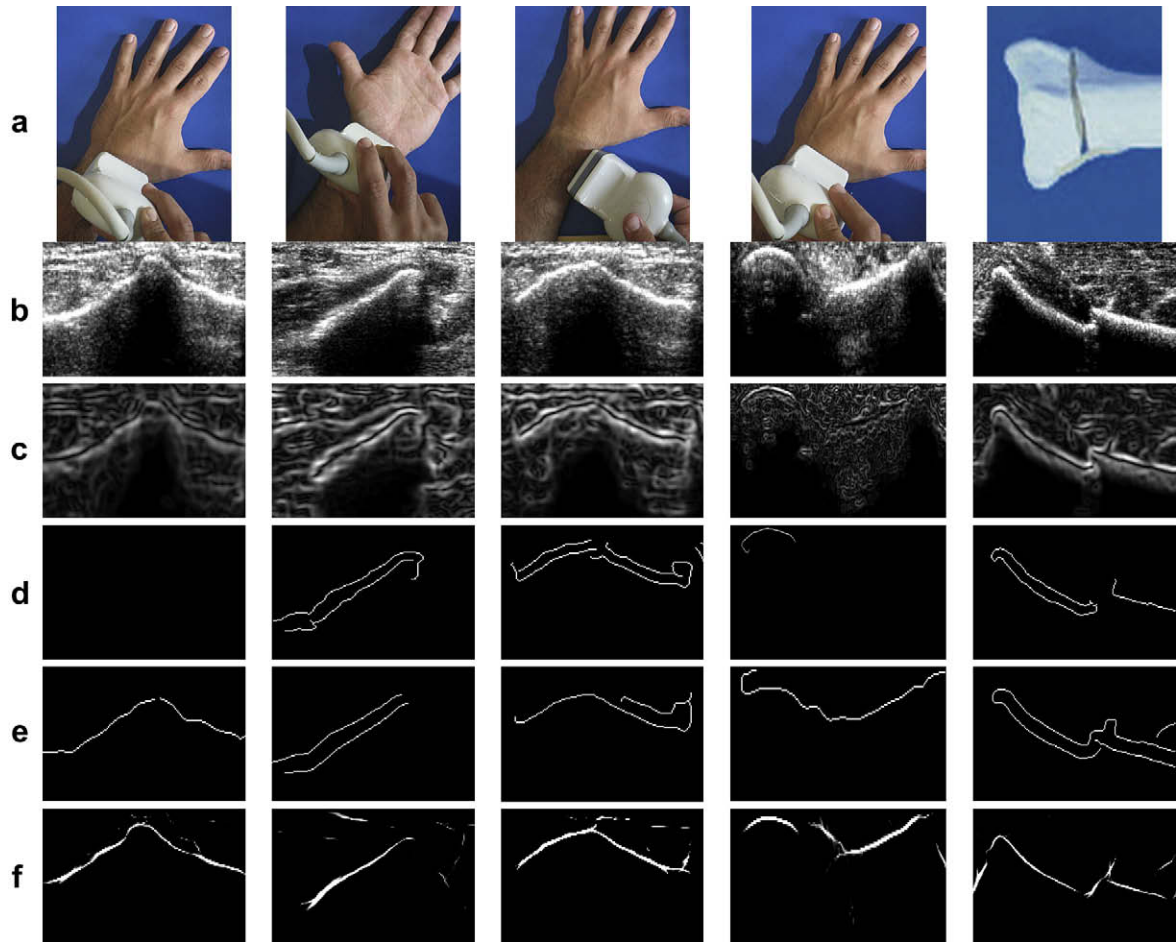


Fig. 12. Qualitative results of the proposed bone localization method in experiment 3. *In vivo* distal radius and ulna images of a normal volunteer and Sawbone imaged with bovine soft tissue overlaid (a) *In vivo* scanning orientation and Sawbone with two-part fracture. (b) B-mode US image. (c) Gradient image obtained using 2-D Gaussian with a standard deviation of two pixels for both directions. (d) Canny image with standard deviation of 2 pixels and %90 threshold value. (e) Canny image with standard deviation of 3 pixels and %80 threshold value. (f) Proposed *PS* image. Columns 1–3 show US images of a distal radius obtained at different probe positions. Column 4 shows an US image of the distal radius and ulna. Column 5 shows a Sawbone with two-part fracture imaged with bovine soft tissue overlaid. Note how our proposed *PS* feature mainly localizes the bone boundaries with little visible influence from US image artifacts, whereas gradient images are influenced strongly by speckle and soft-tissue interfaces. Also note how the Canny edge detector extracts two surfaces, one above and one below the actual bone, because of the thick response of the bone reflection in US. Rows (b) and (c) also show how sensitive the results are to the set parameters except in *PS* images, which were obtained using the same parameter set in all images tested.

As can be observed in Fig. 12, *PS* mostly captured continuous sections of the bone, with little influence exhibited by soft-tissue interfaces, which was not the case for the Canny and gradient images. Furthermore, although *PS* results were noticeably robust and stable, Canny filter results were highly dependent on the choice of parameters, whereas gradient results were strongly influenced by speckle and soft-tissue features. In a number of cases, the Canny edge detector extracted two surfaces, one above and one below the actual bone surface, because of the thick response of the bone reflection in US.

Figure 13 shows a stack of 2-D *PS* images obtained by processing individual 2-D slices from a 3-D US scan.

This result demonstrates how the proposed *PS* features can produce a 3-D surface representation that is relatively continuous and robust in the presence of speckle, shadowing and other ultrasound-specific artifacts. The consistency of the surface produced by *PS* processing as it proceeds from scan to scan along a bone surface suggests the possibility of extending *PS* processing to 3-D US imaging data.

## CONCLUSIONS

Accurate localization of tissue/bone interfaces in US images is a challenging problem that continues to hamper

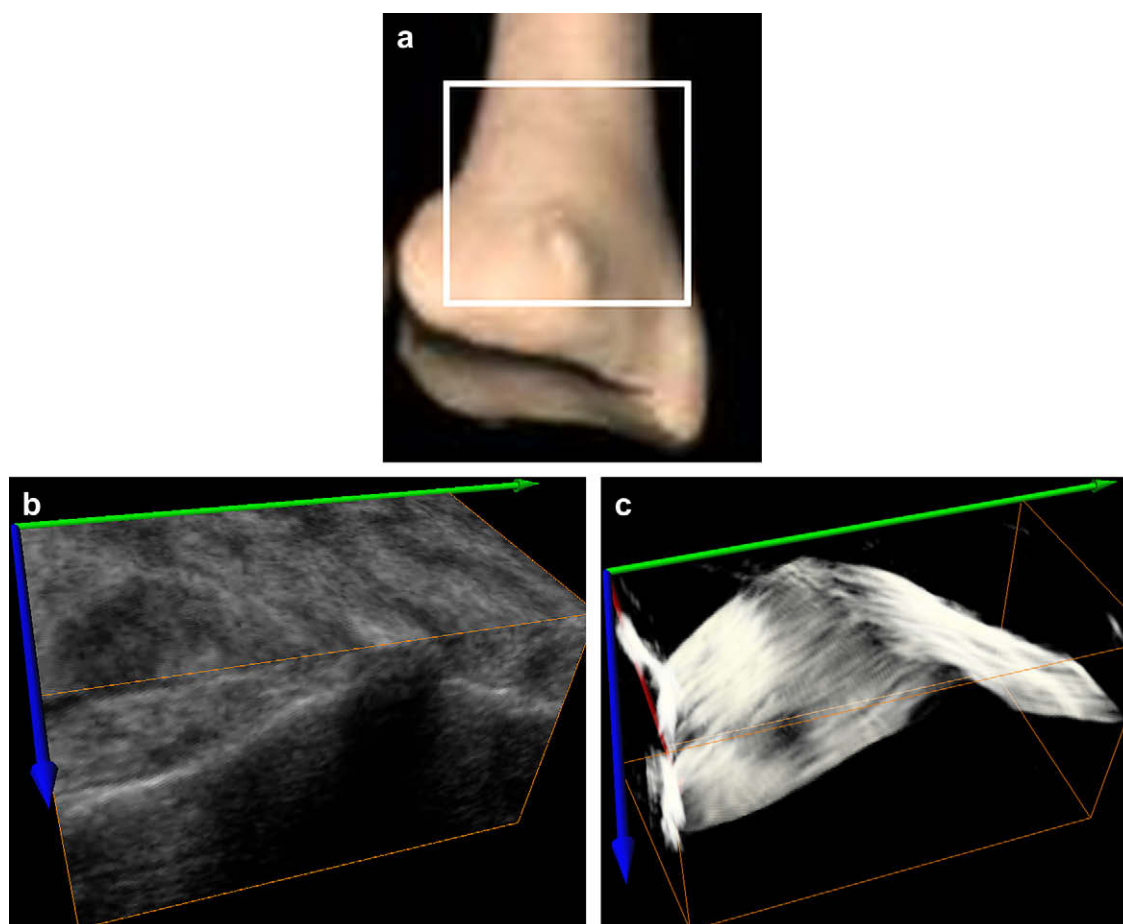


Fig. 13. Qualitative results of the proposed bone localization method in experiment 3, where a stack of 2-D images obtained by scanning an *in vivo* distal radius with a 3-D US probe was processed. (a) 3-D anatomical sketch of a human radius. The scanned area is highlighted by the white rectangle. (b) 3-D US volume of the scanned distal radius. (c) Corresponding 3-D PS image, which shows that the 2D algorithm (after processing individual 2-D slices from a 3-D volume) can produce relatively continuous and clean bone surfaces, with little speckle and US artifacts. This 3-D test is only meant to show how repeatable the *PS* calculations are along a bone surface, which suggests the possibility of extending *PS* processing to 3-D US data.

US deployment in orthopaedic applications. This paper presents a novel approach for automated and accurate bone segmentation from 2-D US images based on local phase information. Phase symmetry extracted using 2-D Log-Gabor filters was proposed as a robust image feature for accurate localization of bone surfaces. Quantitative validation demonstrated submillimeter localization accuracy in phantom studies. Phase information was also shown to be suitable for measuring small bone displacements, also with submillimetric accuracy, a very encouraging finding relevant to applications in fracture assessment and fixation.

In this exploratory work, the *PS* calculations are described, but extension to clinical applications will require modifications of the algorithms for specific clinical tasks. Here, the *PS* feature was defined and the leading edge was extracted. An automatic algorithm may follow this approach that may require more specific definitions

of the decision criteria used to identify the presence of bone or the extent or displacement of a fracture. Additional outlier rejection, incorporation of *a priori* anatomical information when available, preprocessing of the US images, and postprocessing of the *PS* images are also likely to improve the accuracy and robustness of the algorithm.

Our preliminary results on *in vivo* scans of the human distal radius are very encouraging and demonstrate the power of the proposed method in extracting bone surfaces in practical applications in the presence of real soft-tissue interfaces. Our future work will thus focus on applying our presented method to US imaging-based bone fracture assessment and reduction surgery applications. In fact, we have recently obtained ethical approval for a pilot study on bone fracture alignment assessment using US imaging, and will shortly begin investigating the feasibility of our method through clinical analysis and visualization of distal radius and pelvic ring fractures.

**Acknowledgments**—This work was funded in part by the Natural Sciences and Engineering Research Council of Canada (NSERC). The authors would like to thank the surgeon Dr. Pierre Guy from Department of Orthopaedic Surgery, University of British Columbia, for his valuable feedback.

## REFERENCES

- Alfiansyah A, Streichenberger R, Bellemare ME, Coulon O. Automatic segmentation of hip bone surface in ultrasound images using an active contour. *CARS*. 2006. Canada: Montreal, Quebec; June 2006.
- Amin DV, Kanade T, Digioia AM, Jaramaz B. Ultrasound registration of the bone surface for surgical navigation. *J Comput Aid Surg* 2003; 8(1):1–16.
- Barratt DC, Penney PG, Chan SK, Slomczykowski M, Carter TJ, Edwards PJ, Hawkes DJ. Self calibrating 3D-ultrasound-based bone registration for minimally invasive orthopaedic surgery. *IEEE Trans Med Imaging* 2006;25(3):312–323.
- Beek M, Abolmaesumi M, Luenam S, Ellis RE, Sellens RW, Pichora DR. Validation of a new surgical procedure for percutaneous scaphoid fixation using intra-operative ultrasound. *Med Image Anal* 2008;12(2):152–162.
- Boukerroui D, Noble JA, Robini M, Brady M. Enhancement of contrast regions in suboptimal ultrasound images with application to echocardiography. *Ultrasound Med Biol* 2001;27(12):1583–1594.
- Boukerroui D, Noble JA, Brady M. On the choice of band-pass quadrature filters. *J Math Imag Vis* 2004;21:53–80.
- Brendel B, Winter S, Rick A, Stockheim M, Ernert H. Registration of 3D CT and ultrasound datasets of the spine using bone structures. *J Comput Aid Surg* 2002;7(3):146–155.
- Cao G, Shi P, Hu B. Ultrasonic liver discrimination using 2D phase congruency. *IEEE Trans Biomed Eng* 2006;53(10):2116–2119.
- Coppola PT, Coppola M. Emergency department evaluation and treatment of pelvic fractures. *Emerg Med Clin North Am* 2000;18(1):1–27.
- Daanen V, Tonetti J, Troccaz J. A fully automated method for the delineation of osseous interface in ultrasound images. *Proc MICCAI. Lecture Notes in Computer Science* 2004;3216:549–557.
- Field D. Relations between the statistics of natural images and the response properties of cortical cells. *J Opt Soc Am* 1987;4(12):2379–2394.
- Grau V, Noble AJ. Adaptive multiscale ultrasound compounding using phase information. *Proc MICCAI. Lecture Notes in Computer Science* 2005;3749:589–596.
- Hacihaliloglu I, Abugharbieh R, Hodgson AJ, Rohling RN. Enhancement of bone surface visualization from 3D ultrasound based on local phase information. *Proc IEEE Ultrason Symp* 2006;21–24.
- Hanel DP, Jones MD, Trumble TE. Wrist fractures. *Orthop Clin North Am* 2002;33(1):35–57.
- He P, Zheng J. Segmentation of tibia bone in ultrasound images using active shape models. *Proc IEEE-EMBS* 2001;3:2712–2715.
- Jain AK, Taylor RH. Understanding bone responses in B-mode ultrasound images and automatic bone surface extraction using a Bayesian probabilistic framework. *Proc SPIE Med Imag* 2004;5733:131–142.
- Kovesi PD. Invariant measures of image features from phase information. Ph.D. thesis. Australia: University of Western Australia; 1996.
- Kovesi P. Symmetry and Asymmetry from Local Phase. *Proc Tenth Australian Joint Conference on Artificial Intelligence* 1997;185–190.
- Kovesi P. Image features from phase congruency. *J Comp Vis Res* 1999; 1(3):1–26.
- Kowal J, Amstutz C, Langlotz F, Talib H, Ballester MG. Automated bone contour detection in ultrasound B-mode images for minimally invasive registration in computer assisted surgery an in vitro evaluation. *Int J Med Robot Comput Assist Surg* 2007;3(4):341–348.
- Kryvanos A. Computer assisted surgery for fracture reduction and deformity correction of the pelvis and long bones. PhD thesis. Germany: University of Mannheim; 2002.
- McMurtry RY, Jupiter JB, Browner BD. Fractures of the distal radius. *Skeletal Trauma: Fractures, Dislocations, Ligamentous Injuries* 1997;1063–1091.
- Mellor M, Brady M. Phase mutual information as a similarity measure for registration. *Med Imag Anal* 2005;9(4):330–343.
- Morrone MC, Owens RA. Feature detection from local energy. *Pattern Recogn Lett* 1987;6(5):303–313.
- Mulet-Parada M, Noble JA. 2D+T boundary detection in echocardiography. *Med Imag Anal* 2000;4(1):21–30.
- Oppenheim AV, Lim JS. The importance of phase in signals. *Proc IEEE* 1981;69(5):529–541.
- Penney GP, Barratt DC, Chan CSK, Slomczykowski M, Carter TJ, Edwards PJ, Hawkes DJ. Cadaver validation of intensity-based ultrasound to CT registration. *Med Imag Anal* 2006;10(3):385–395.
- Phillips R. The accuracy of surgical navigation for orthopaedic surgery. *Curr Orthop* 2007;21(3):180–192.
- Rohling R, Munger P, Hollerbach J, Peters TM. Comparison of relative accuracy between a mechanical and an optical position tracker for image-guided neurosurgery. *J Imag Guided Surg* 1995;1(1):30–34.
- Sanchez-Ortiz G, Declerck J, Mulet-Parada M, Noble JA. Automatic 3D echocardiographic image analysis. *Proc MICCAI 2000. Lecture Notes in Computer Science* 1935:687–696.
- Tonetti J, Carrat L, Blendea S, Merloz P, Troccaz J, Lavallee S, Chirossel JP. Clinical results of percutaneous pelvic surgery: Computer assisted surgery using ultrasound compared to standard fluoroscopy. *J Comput Aid Surg* 2001;6(4):204–211.
- Ye X, Noble JA. 3D freehand echocardiography for automatic left ventricle reconstruction and analysis based on multiple acoustic windows. *IEEE Trans Med Imag* 2002;21(9):1051–1058.